nature communications

Article

https://doi.org/10.1038/s41467-025-57643-7

Robust Fe-N_4-C_6O_2 single atom sites for efficient PMS activation and enhanced $Fe^{IV}=O$ reactivity

Received: 28 June 2024

Accepted: 26 February 2025

Published online: 10 March 2025

Check for updates

Tiantian Chen[1], Ganbing Zhang[2] ✉, Hongwei Sun[1], Yetong Hua[1], Shu Yang[1], Dandan Zhou[1], Haoxin Di[1], Yiling Xiong[1], Shenghuai Hou[1], Hui Xu[1] ✉ & Lizhi Zhang[3] ✉

The microenvironment regulation of Fe-N_4 single atom catalysts (SACs) critically governs peroxymonosulfate (PMS) activation. Although conventional heteroatom substitution in primary coordination enhances activity, it disrupts Fe-N_4 symmetry and compromises stability. Herein, we propose oxygen doping in the secondary coordination shell to construct Fe-N_4-C_6O_2 SAC, which amplifies the localized electric field while preserving the pristine coordination symmetry, thus trading off its activity and stability. This approach suppresses Fe-N bond structural deformation (bond amplitude reduced from 0.875–3.175 Å to 0.925–2.975 Å) during PMS activation by lowering Fe center electron density to strengthen Fe-N bond, achieving extended catalytic durability (>240 h). Simultaneously, the weakened coordination field lowers the Fe=O σ* orbital energy, promoting electrophilic σ-attack of high-valent iron-oxo towards bisphenol A, and increasing its degradation rate by 41.6-fold. This work demonstrates secondary coordination engineering as a viable strategy to resolve the activity-stability trade-off in SAC design, offering promising perspectives for developing environmental catalysts.

Advanced oxidation processes (AOPs) based on peroxymonosulfate (PMS) have attracted great attention for pollutant control and environmental remediation due to their high efficiency in a wide pH range[1]. Recently, single-atom catalysts (SACs) with metal-N_4 (M-N_4) sites, where the metal centers are coordinated with four nitrogen atoms, are widely used for the PMS activation because of their outstanding catalytic activity, excellent selectivity, and exceptionally high metal utilization efficiency[2–5]. The electron donating potential of these M-N_4 sites can trigger the PMS activation to produce sulfate radicals ($SO_4^{\bullet-}$), hydroxyl radicals (•OH), and high-valence metal-oxo ($M^{IV}=O$), etc., thus effectively facilitating the degradation of various organic pollutants[6–14]. However, the high bond dissociation energies of O-H and O-O bonds in PMS pose a significant challenge to their cleavage, thereby disfavoring the PMS activation at M-N_4 sites[15]. Therefore, the development of high-performance catalysts to promote the PMS activation is crucial for the effective oxidation of contaminants.

Recently, many strategies have been proposed for the efficient PMS activation via increasing the density of metal centers or regulating their local environment surrounding in metal-SACs (M-SACs)[16–19]. Among these strategies, the most common one is the partial replacement of N in the first coordination shell with foreign elements, thereby creating an enhanced localized electric field to facilitate the activation

[1]State Key Laboratory of Green Pesticide; Engineering Research Center of Photoenergy Utilization for Pollution Control and Carbon Reduction, Ministry of Education; College of Chemistry, Central China Normal University, Wuhan, PR China. [2]Collaborative Innovation Center for Advanced Organic Chemical Materials Co-constructed by the Province and Ministry; Ministry-of-Education Key Laboratory for the Synthesis and Applications of Organic Functional Molecules; College of Chemistry and Chemical Engineering, Hubei University, Wuhan, PR China. [3]School of Environmental Science and Engineering, National observation and Research Station of Erhai Lake Ecosystem in Yunnan, Yunnan Dali Research Institute, Shanghai Jiao Tong University, Shanghai, PR China. ✉e-mail: gbzhang@hubu.edu.cn; huixu@ccnu.edu.cn; zhanglizhi@sjtu.edu.cn

of O-H and O-O bonds in PMS[20,21]. Unfortunately, this strategy destroys the symmetric structure of M-N_4 sites, potentially decreasing their long-term stability via the accelerated demetallation. For instance, Dai et al. found that the catalytic activity of Fe-S_1N_3-C significantly diminished after two cycles of reaction within 60 min[22]. Peng's group demonstrated that FeN_2O_2 could remove all paracetamol within 40 min, but complete degradation of paracetamol was not realized even after extending the reaction time to 180 min at the second reuse cycle[23]. Therefore, it is still a great challenge to balance the high activity and the long durability of SACs for the PMS activation.

Different from the first coordination shell doping, the heteroatom doping in the second coordination shell of M-N_4 sites could improve the catalytic performance of M-N_4 sites by modulating the electronic structure of the metal center through d-p long-range interactions, and simultaneously maintain the M-N_4 coordination structure[24–27]. For instance, the electron-withdrawing effect of S doping in the second coordination shell was demonstrated to be beneficial for anchoring single Fe atoms, significantly enhancing the nitrate electroreduction activity and stability of Fe-N_4 sites in comparison with Fe-plate. However, the influence of S doping shell location on the catalytic stability of Fe-N_4 sites was not investigated[24]. In comparison with nitrate electroreduction, the PMS activation imposes much stricter requirements on the catalytic stability of Fe-N_4 sites owing to its strong oxidative environment. Regarding that the electronegativity of O (3.44) is higher than that of S (2.58), we anticipate that the O doping can reduce the electron density in the metal center more significantly through d-p long-range interaction and establish a stronger electric field gradient around M-N_4 sites, facilitating the adsorption and activation of negatively charged PMS (HSO_5^-). Meanwhile, the O doping in the second coordination shell might favor the formation of carbon vacancies around the metal center and alter the binding ability between the metal and surrounding coordination atoms, thus suppressing demetallation.

Herein, we develop a pre-coordination strategy to engineer heteroatom doping by precisely controlling the substitution of neighboring first coordination shell N atoms and distanced second coordination shell C atoms of Fe center, aiming to clarify the effects of O doping in the first or second coordination shell on the reactivity and stability of Fe-N_4 sites through systematical characterization, degradation experiments, density functional theory (DFT) calculations and molecular dynamics (MD) simulations. This study sheds light on the design of SACs with enhanced PMS activation performance by addressing the trade-off between activity and sustainable stability.

Results

Synthesis and characterization

Fe-SACs with oxygen doped in the first (Fe-N_2O_2-C_{10}) or the second shell (Fe-N_4-C_6O_2) were synthesized by a pre-coordination strategy (Fig. 1a). First, we synthesized two core-shell structured carriers with utilizing silica (SiO_2) as the core layer. One of shell layers was composed of nitrogen-doped carbon (N-C) without any oxygen functional groups (SiO_2@N-C), while the other consisted of resorcinol-formaldehyde (RF) enriched with oxygen functional groups (SiO_2@RF) (Supplementary Fig. 1a–c). Meanwhile, Fe-N/O co-coordination (I) and Fe-N coordination (II) complexes were prepared using (S, S)-(+)-N, N′-bis(3,5-di-tert-butylsalicylidene)-1, 2-cyclohexanediamin as the N/O precursors and 1,10-phenanthroline as the N precursor, respectively. Subsequently, complexes (I) and (II) were deposited on SiO_2@N-C and SiO_2@RF using the rotary evaporation technique, which were then subjected to the processes of high-temperature pyrolysis and SiO_2 template removal to obtain Fe-N_2O_2-C_{10} and Fe-N_4-C_6O_2, respectively. Fe-SAC without O-doping (Fe-N_4-C_{10}) was also synthesized with the same procedure except for the deposition of complex (I) on SiO_2. For comparison, N/O co-doped carbon (N/O-C), N-C, and Fe nanoparticles supported on N-doped C (Fe NPs/NC) were also fabricated (Supplementary Table 1).

All the three Fe-SACs were of ultrathin, uniform, hierarchically porous hollow structure (Fig. 1b and Supplementary Figs. 1–3), facilitating the full exposure of active sites and the mass transfer during the PMS activation. Their powder X-ray diffraction (PXRD) patterns only contained one broad peak at 25° corresponding to the (002) plane of the carbon carrier, without any discernible peaks arisen from crystalline iron or iron oxides (Fig. 1c)[28]. Meanwhile, the existence of iron particles was ruled out by their high-resolution transmission electron microscope (HR-TEM) images and the selected area electron diffraction (SAED) patterns (Supplementary Fig. 1). Aberration-corrected high-angle annular dark field scanning electron microscopy (AC-HAADF STEM) images of Fe-N_4-C_6O_2 clearly indicated that bright spots of sizes, consistent with single Fe atoms (1.002 ± 0.173 Å), were uniformly dispersed in the dark O-N/C background (Fig. 1d, e)[6], confirming the atomically dispersion of Fe.

We then checked the electronic structure and coordination environment of Fe atoms in three Fe-SACs by X-ray absorption fine structure, X-ray photoelectron spectroscopy (XPS), and ^{57}Fe Mössbauer spectroscopy. As shown in X-ray absorption near-edge structure (XANES) spectra (Fig. 2a), the pre-edge peak and absorption edge of Fe-N_2O_2-C_{10} and Fe-N_4-C_6O_2 shifted towards higher energies, accompanied by the intensity increase of the white-line peak, indicating that the O doping altered the coordination environment of Fe centers and reduced their electron densities[15,29]. Obviously, these changes were more pronounced in the XANES spectrum of Fe-N_2O_2-C_{10}, indicative of its shorter distance and stronger interaction between O and Fe. The Fourier-transformed k^3-weighted extended X-ray absorption fine structure (FT-EXAFS) spectrum of Fe-N_2O_2-C_{10} revealed a broad and unsymmetric peak with the peak maximum located at 1.44 Å, close to the Fe-O backscattering, indicating the presence of Fe-N and Fe-O dual coordination in Fe-N_2O_2-C_{10} (Fig. 2b). Similar results were found in the recent reports on Fe-N_3S_1, Co-N_2O_2, Co-N_3O_1, and Fe-N_2O_2[22,30–32]. Differently, the main peak of Fe-N_4-C_6O_2 and Fe-N_4-C_{10} were symmetric and left-shifted to ~1.4 Å, belonging to the single Fe-N scattering path. However, a new peak in the 1–2 Å range of R-space appeared in the spectrum of Fe-N_4-C_6O_2, indicating that the different coordination environments of Fe-N_4-C_6O_2 and Fe-N_4-C_{10}. These results confirmed that O was doped into outer coordination shells of $n \geq 2$ in Fe-N_4-C_6O_2. Moreover, those peaks with R > 2 Å (pentagram markers) could not be assigned to Fe-Fe scattering path, because the wavelet transforms (WT) EXAFS contours of three Fe-SACs samples had only one intensity maximum corresponding to the Fe-N/O coordination at **k** value of 5 $Å^{-1}$ in the R range of 1–3 Å (Fig. 2c). Subsequently, quantitative least-squares fitting of the FT-EXAFS curves revealed that the optimal coordination numbers of Fe in all three Fe-SACs were approximately 4 (Fig. 2d, Supplementary Fig. 4 and Table 2). The distinction lied in the fact that Fe-N_2O_2-C_{10} encompassed both Fe-N and Fe-O backscattering paths, thereby confirming the successful construction of a Fe-N/O dual coordination environment[32], while the other two Fe-SACs solely exhibited Fe-N backscattering paths. As expected, two distinct and equally proportioned Fe-N bond lengths of 1.91 Å and 2.09 Å were observed in Fe-N_4-C_6O_2, indicating that the two O atoms were doped into the second coordination shell, consistent with the reported results of Fe-N_4-S_2 with S doped in the second coordination shell[24,26]. Contrarily, Fe-N_4-C_{10} SAC without O doping showed only one set of Fe-N bonding length at 1.97 Å.

We further characterized Fe-N_4-C_6O_2 and Fe-N_4-C_{10} using ^{57}Fe Mössbauer spectroscopy to elucidate their coordination environments of Fe. Their deconvoluted ^{57}Fe Mössbauer spectra exclusively exhibited doublets, without any singlet or sextet associated with α-Fe, Fe_xC, or Fe_xO (Fig. 2e, f). According to the isomer shift (δ_{iso}) and quadrupole splitting (ΔE_Q) values, ^{57}Fe Mössbauer spectrum of Fe-N_4-C_6O_2 could be well fitted with three doublets (D1-D3), corresponding

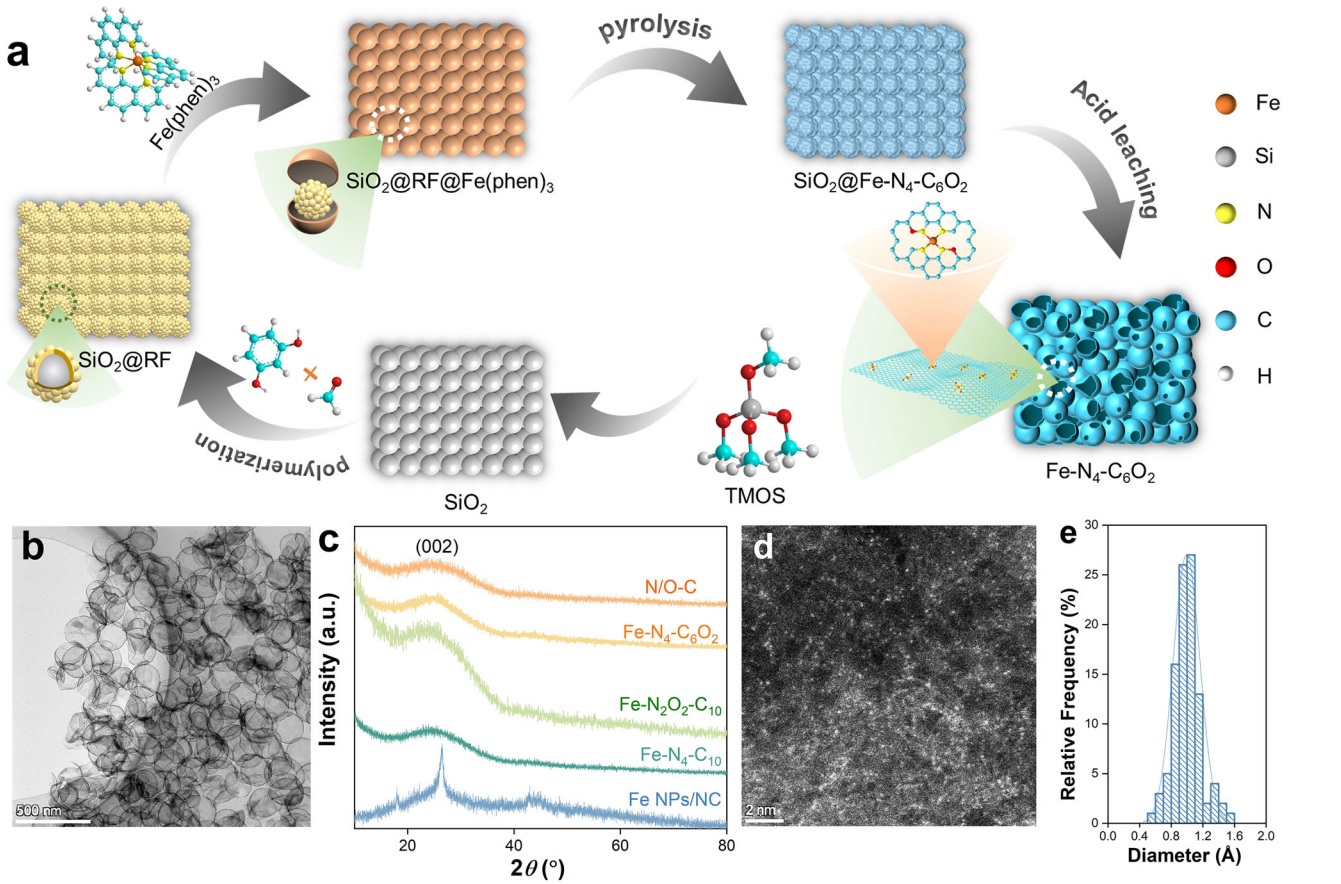

Fig. 1 | Synthesis and characterization of Fe-SACs. a Schematic diagram of the Fe-N_4-C_6O_2 synthesis. **b** TEM images of Fe-N_4-C_6O_2. **c** PXRD pattern of different catalysts. **d** HADDF-STEM images of Fe-N_4-C_6O_2. **e** The particle size of Fe in Fe-N_4-C_6O_2. Source data are provided as a Source Data file.

to medium-spin (MS) $Fe^{II}N_{2+2}$ (D1), medium-spin (MS) $Fe^{III}N_{2+2}$ (D2), and high-spin (HS) N-$Fe^{II}N_{2+2}$ (D3), respectively (Supplementary Table 3)[33–35], wherein Fe-N_{2+2} represents the defective Fe-N_4 site in the non-intact graphite layer structure (Supplementary Fig. 5). In contrast, four different doublets (D4-D7) could be identified in Fe-N_4-C_{10}, which were assigned to low-spin (LS) $Fe^{III}N_4$/C (D4), LS $Fe^{II}N_4$/C (D5), MS $Fe^{II}N_4$/C (D6), and HS $Fe^{II}N_4$/C (D7), respectively[13,33,36]. The relatively higher intensity ratio of D-band to G-band (I_D/I_G = 1.07) in Fe-N_4-C_6O_2 than that of Fe-N_4-C_{10} (0.94) evidenced that the O doping created more defects (Supplementary Fig. 6). Meanwhile, the presence of Fe-N and N-O bonds were also confirmed by HR-XPS spectra of Fe 2*p*, N 1*s*, and O 1*s* in Fe-N_4-C_6O_2 (Supplementary Figs. 7–8). Therefore, we concluded that two O atoms were doped in the second coordination shell of Fe-N_4-C_6O_2.

Considering the presence of doped O atoms in the second coordination shell of Fe-N_4-C_6O_2, we constructed three possible Fe-N_4-C_6O_2 models using DFT (Fig. 2g). Specifically, the two O atoms could be situated at either ipsilateral a and b positions (configuration I), or ipsilateral b and c positions (configuration II), or opposite b and d positions (configuration III) within the second coordination shell, respectively. However, the optimization of configuration I led to the connection of C atoms at positions c and d, which contradicted the Fe-N_{2+2} structure and consequently resulted in its exclusion. The stability of configuration II was significantly lower than that of configuration III, despite its conformity to the requirements for the Fe-N_{2+2} structure. Therefore, configuration III was selected as the Fe-N_4-C_6O_2 model in this study. The formation of configuration III could be attributed to the thermal rearrangement of atoms during pyrolysis (Supplementary Fig. 9). The stably coordinated Fe-N precursor prevented O atoms entering the first coordination shell, and providing more opportunity for them to replace C_1 atoms in the second coordination shell of Fe-N_4. Subsequently, the eight-electron rule and high electronegativity of the O atoms led to the loss of a linkage of the C_2 atoms and a deviation in Fe-N bond length[26]. Eventually, the collision of C_2 atoms with N_2 molecules in irregular thermal motion would lead to their release from the catalyst surface to form carbon vacancies (CVs), accompanying with a configuration transformation from Fe-N_4 to Fe-N_{2+2}. Different from Fe-N_4-C_{10}, Fe-N_4-C_6O_2 possessed much enhanced Lorenz curve signal, indicative of more unpaired electrons in Fe-N_4-C_6O_2 (Fig. 2h), which contributed to improving the electron transfer efficiency during the catalytic reaction. The increase in unpaired electron could be attributed to the O introduction and the CVs formation. The O introduction could effectively weaken the ligand field, increasing the spin state and the number of unpaired electrons in the Fe center (Supplementary Table 3). The CVs formation via the loss of C atoms would leave extra electrons redistribute among neighboring C atoms to form more unpaired electrons[37,38]. Furthermore, the natural population analysis (NPA) charge and partial density of state (PDOS) analysis revealed that the O doping in the second coordination shell reduced the electron density of Fe atom and narrowed its d-band width via changing the electronic structure of N ligand (Fig. 2i and Supplementary Fig. 10)[39,40], thus shifting the d-band center of Fe in Fe-N_4-C_6O_2 (−1.842 eV vs −2.137 eV for Fe-N_4-C_{10}) closer to the Fermi level (E_f) (Fig. 2i), and enhancing the intrinsic reactivity of Fe-SAC towards the PMS activation.

PMS activation and pollutant degradation

We utilized DFT calculations to investigate the influence of O doping on the PMS activation and the reactive oxygen species (ROS) formation, and employed an asterisk (*) to denote the surface adsorbed

https://doi.org/10.1038/s41467-025-57643-7

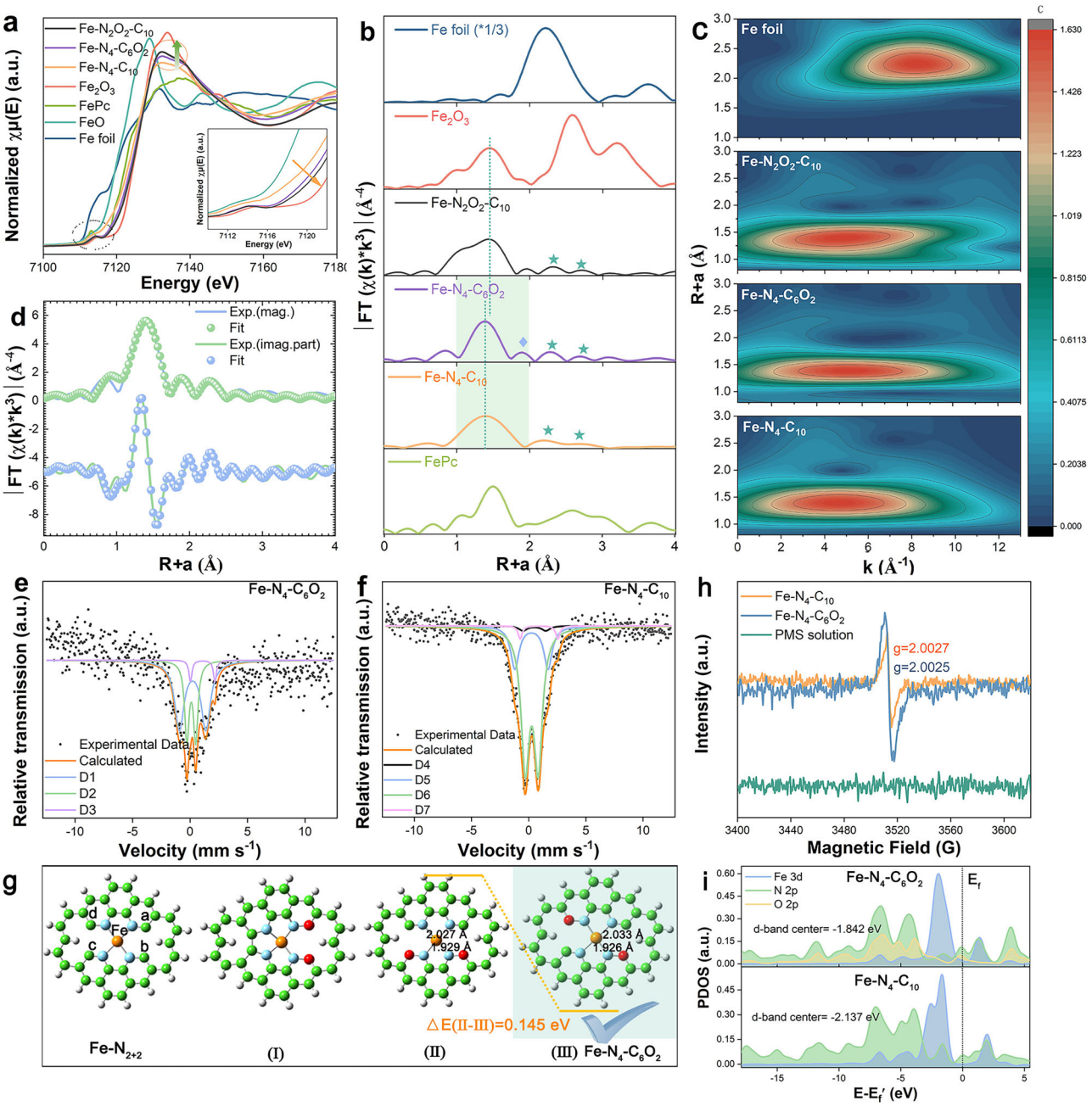

Fig. 2 | Spectroscopic characterization and structural calculation of catalysts. **a** XANES (inset: magnified view of XANES), **b** FT-EXAFS spectra (k^3-weighted), and **c** WT-EXAFS spectra of different Fe foil and Fe-SACs. **d** Corresponding EXAFS R-space fitting curve of Fe-N_4-C_6O_2. ^{57}Fe Mössbauer spectroscopy of **e** Fe-N_4-C_6O_2 and **f** Fe-N_4-C_{10}. **g** Optimized geometries of three types possible Fe-N_4-C_6O_2 active site structure. **h** EPR spectra and **i** PDOS of Fe-SACs[55]. Source data are provided as a Source Data file.

species and $O_1/O_2/O_3$ to represent the three different types of oxygen atoms in PMS (Supplementary Figs. 11–12). As expected, the higher positive charge of Fe center and its surrounding strong local electric field in Fe-N_2O_2-C_{10} promoted the PMS adsorption and triggered the rapid cleavage of peroxide (O_2-O_3) bond (Fig. 3a), while the low electron density of Fe center facilitated its robust interaction with $O_1/O_2/O_3$, delocalizing Fe atom from the carrier plane and elongating the Fe-N and Fe-O bonds to 2.161–2.826 Å to potentially result in demetallation. However, the reduction of positive charge on Fe centers and their surrounding local electric field in Fe-N_4-C_6O_2 and Fe-N_4-C_{10} failed to satisfy the requirements for direct breakage of O_2-O_3 bond induced by their PMS adsorption, and thus might form complexes (I), (II), and (III) with PMS via O_1, O_2, and O_3, respectively (Fig. 3a and Supplementary Fig. 11), while the activation of the O_2-O_3 bond only occurred in complex (III). Therefore, complex (III) was adopted for the following calculations.

Subsequently, the formation of high-valent iron-oxo (Fe^{IV}=O) and radicals in the three Fe-SACs/PMS systems was explored theoretically. As shown in Fig. 3b, c, it was also thermodynamically feasible for the generation of Fe^{IV} = O in the Fe-N_2O_2-C_{10}/PMS system via the traditional pathway of *(I) → *PMS (II) → *OH (III) → *OH*OH (IV) → transition state (TS, V) → *O*H_2O (VI) → *O (VII)[41]. Differently, the appropriate distance between O_1 and H of *PMS(Fe-N_4-C_6O_2) and *PMS(Fe-N_4-C_{10}) facilitated the formation of intramolecular hydrogen bonds, and the interaction between Fe and O_3 weakened the O_2-O_3 and O_3-H bonds, thus favoring their cleavage to produce Fe^{IV} = O through the non-classical coupled

https://doi.org/10.1038/s41467-025-57643-7

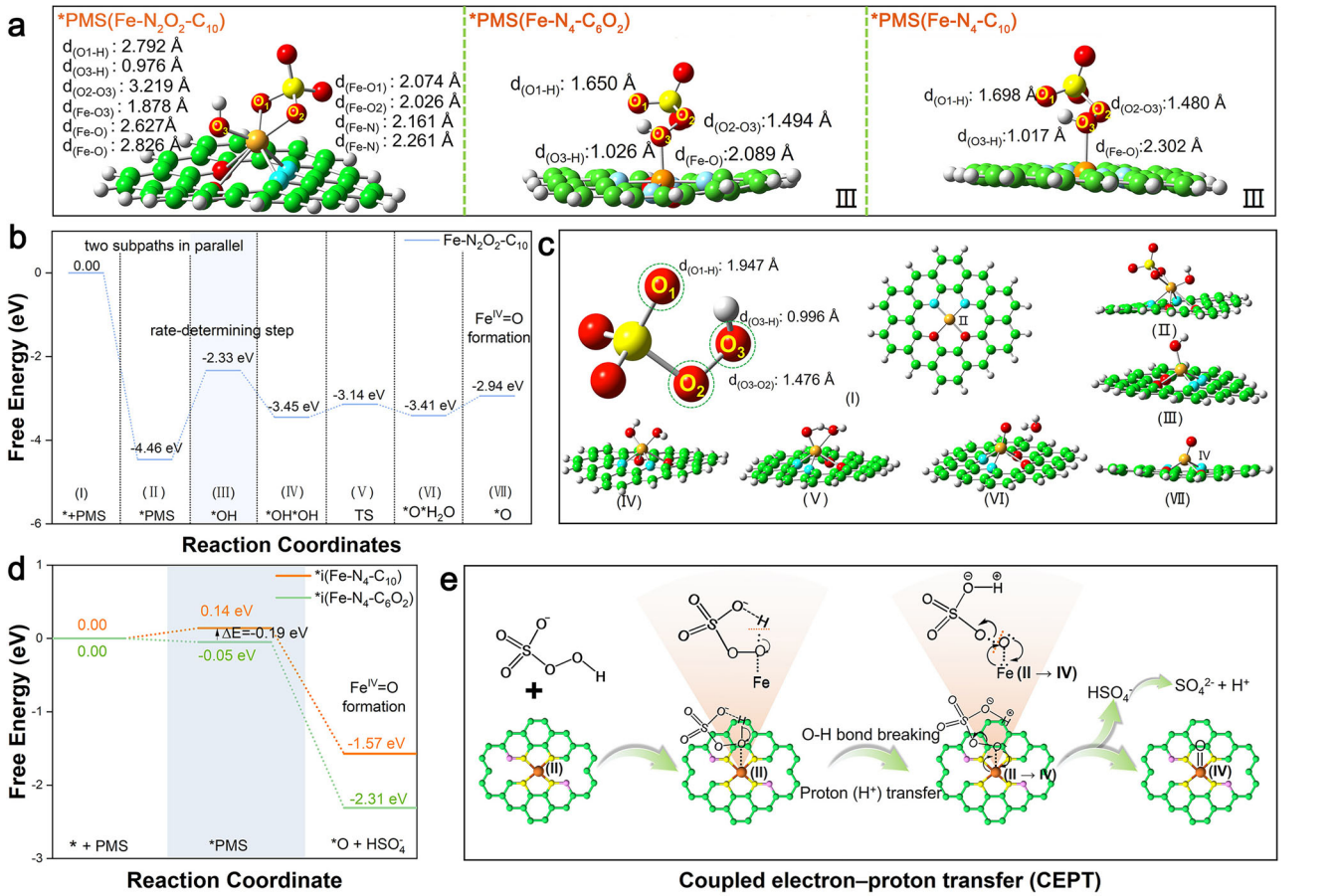

Fig. 3 | Molecular mechanism of PMS activation on Fe-SACs. a The adsorption configuration of PMS on Fe-SACs. **b** The free energy for the $Fe^{IV}=O$ generation in the Fe-N_2O_2-C_{10}/PMS system. **c** The structures of intermediates during $Fe^{IV}=O$ formation in the Fe-N_2O_2-C_{10}/PMS system. **d** The free energies for the $Fe^{IV}=O$ generation in the Fe-N_4-C_6O_2/PMS and Fe-N_4-C_{10}/PMS systems. **e** The schematic diagram of the CEPT. Source data are provided as a Source Data file.

electron-proton transfer (CEPT) pathway (Fig. 3d, e and Supplementary Fig. 12)[21]. In this pathway, protons were easily transferred from O_3 to O_1, and the two remaining electrons in the O_3 2p orbital would be coupled with the two electrons of Fe to form the Fe=O bond. Notably, the distantly doped O and CVs promoted the PMS adsorption by lowering the adsorption energy from −0.21 eV for Fe-N_4-C_{10} to −0.46 eV for Fe-N_4-C_6O_2 (Supplementary Fig. 12), and affected the *PMS structure by providing a moderately enhanced local electric field, including elongated O_2-O_3 (1.494 Å for Fe-N_4-C_6O_2 vs 1.480 Å for Fe-N_4-C_{10}) and O_3-H (1.026 Å for Fe-N_4-C_6O_2 vs 1.017 Å for Fe-N_4-C_{10}) bonds, as well as a reduced distance between O_1 and H (1.650 Å for Fe-N_4-C_6O_2 vs 1.698 Å for Fe-N_4-C_{10}). These changes effectively improved the thermodynamic (−2.31 eV for Fe-N_4-C_6O_2 and −1.57 eV for Fe-N_4-C_{10}) and kinetic possibilities of the Fe-N_4-C_6O_2/PMS system for the $Fe^{IV}=O$ generation via CETP pathway. Finally, the thermodynamic feasibility of radical formation in three Fe-SACs/PMS systems through the single electron transfer pathway was calculated, obeying the trend of Fe-N_2O_2-C_{10}/PMS with Gibbs free energy (ΔG) of −1.21 eV > Fe-N_4-C_{10}/PMS with ΔG of −0.70 eV > Fe-N_4-C_6O_2/PMS with ΔG of −0.41 eV (Supplementary Fig. 13). However, the significantly lower ΔG associated with the $Fe^{IV}=O$ formation (−2.94 eV for Fe-N_2O_2-C_{10}, −2.31 eV for Fe-N_4-C_6O_2, −1.57 eV for Fe-N_4-C_{10}) suggested that the $Fe^{IV}=O$ formation was much easier than that of radicals in three Fe-SACs/PMS systems.

We then evaluated the PMS activation performance of Fe-SACs by the bisphenol A (BPA) removal, and found that the O doping significantly enhanced the activity of Fe-SACs and N/O-C, while Fe-N_4-C_6O_2 exhibited the best catalytic activity among the three Fe-SACs samples (Fig. 4a and Supplementary Fig. 14). BPA could be completely removed in 30 s with a pseudo-first-order rate constant (k) as high as 13.299 min^{-1} at 0.1 mg mL^{-1} of Fe-N_4-C_6O_2 and 400 μM of PMS (Fig. 4a and Supplementary Fig. 15). Impressively, the BPA removal performance of Fe-N_4-C_6O_2 even surpassed those of homogeneous Fe^{2+}, commercial Fe_3O_4 and Fe NPs/NC, nZVI/kaolinite, and other reported M-SACs (Fig. 4b and Supplementary Fig. 16). More importantly, Fe-N_4-C_6O_2 displayed broad pH compatibility and maintained >85% contaminant removal efficiency under high-concentration inorganic ions interference and common water matrices (Supplementary Fig. 17). Moreover, the Fe-N_4-C_6O_2/PMS system could effectively remove various pollutants (Supplementary Table 4), but their degradation rates were affected by their structures. For example, electron-rich phenolic pollutants such as 2, 4-dichlorophenol (2, 4-DCP), p-chlorophenol (4-CP), and phenol (PE) were completely degraded within 1.5 min, with the pseudo-first-order rate constant (k) ranging from 5.522 to 10.877 min^{-1} (Supplementary Fig. 18). Nevertheless, contaminants with electron-withdrawing groups, such as p-nitrophenol (PNP), fipronil (FP), p-nitrobenzyl alcohol (PNBA), and p-nitrobenzaldehyde (PNBD), were difficult to be completely degraded within 20 min even at a high PMS concentration of 3 mM, and the k values were as low as 0.0944–1.6274 min^{-1}. The high selectivity towards electron-rich pollutants indicated that non-radical reactive oxidation may be dominant in this system[41].

Notably, the activities of N/O-C and N-C were significantly lower than those of the three Fe-SACs (Supplementary Fig. 14), thus confirming that atomically dispersed Fe sites play an indispensable role in the effective PMS activation. Therefore, the specific activity of individual Fe site was further investigated, and the BPA turnover frequency

https://doi.org/10.1038/s41467-025-57643-7

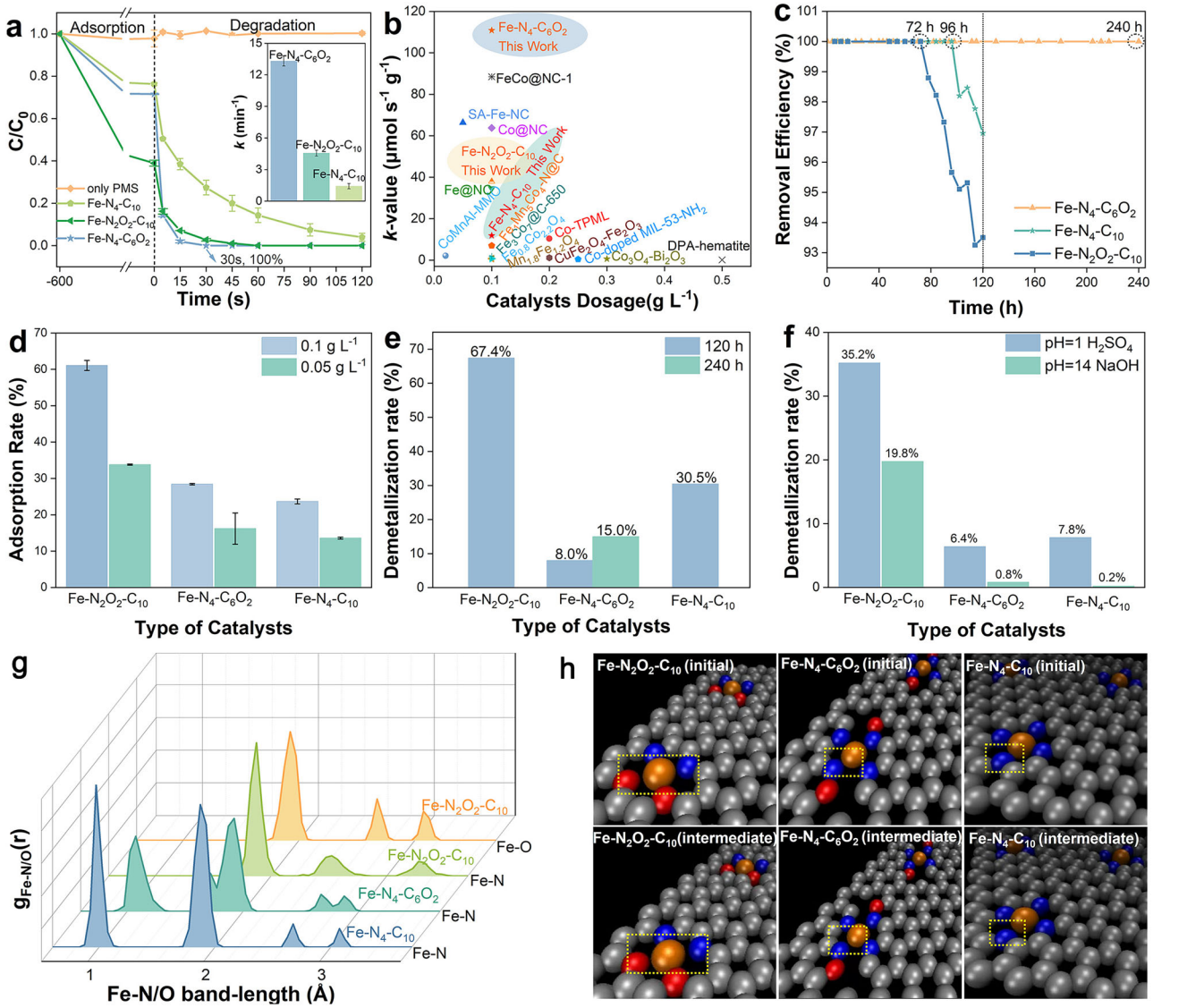

Fig. 4 | Activity and stability evaluation of Fe-SACs. a The degradation of BPA in different catalysts-activated PMS systems (inset: corresponding pseudo-first-order rate constant of BPA removal). The error bars represent the standard deviation derived from two repeated experiments. Experimental conditions: [Catalysts] = 0.1 g L^{-1}, [BPA] = 50 μM, $[PMS]_0$ = 400 μM, T = 25 °C, pH = 7. **b** The catalyst dose-pollutant concentration normalized kinetic rate constant (*k*-value) of BPA removal in different catalysts/PMS systems. **c** Continuous operation test of BPA degradation in the continuous flow system. Average flow rate: 45 L m^{-2} h^{-1}, catalyst dosage: 20 mg. **d** The adsorption rate of Fe-SACs on BPA at different dosages. The demetallation rates of different Fe-SACs after (**e**) continuous removal of BPA for 120 h and 240 h and (**f**) 36 h of corrosion by strong acids/bases. **g** Fe-N and Fe-O radical distribution function profiles of Fe-SACs at 25 °C. **h** Snapshots of Fe-SACs obtained from MD simulations at 25 °C. The initial configuration and an intermediate state are provided to show the elongation of the Fe−N/Fe-O bond as marked by the yellow box. Source data are provided as a Source Data file.

(TOF) of Fe sites was in the order of Fe-N_2O_2-C_{10} > Fe-N_4-C_6O_2 > Fe-N_4-C_{10}, which suggested that the O doping in the first coordination shell could enhance the activity of Fe sites more effectively than the O doping in the second coordination shell (Supplementary Fig. 19). This is attributed to the doped oxygen in Fe-N_2O_2-C_{10} significantly reduced the electron density of the Fe center and created a stronger local electric field around it via direct interactions and disruption of the Fe-N_4 symmetric coordination structure, thus enhancing the adsorption and activation of negatively charged PMS, consistent with theoretical calculations. Although the TOF of iron sites in Fe-N_2O_2-C_{10} was 10.6 times higher than that in Fe-N_4-C_6O_2, the iron content in Fe-N_2O_2-C_{10} (0.196 wt%) was only 7.5% of that in Fe-N_4-C_6O_2 (2.63 wt%, Supplementary Table 5), resulting in the lower apparent activity of the former (Fig. 4a). Next, we attempted to increase the Fe content of Fe-N_2O_2-C_{10} by increasing the proportion of Fe precursors, which instead resulted in its significant metal agglomeration and catalytic reactivity decrease (Supplementary Fig. 20), suggesting that the O doping in the first coordination shell disfavored the stability of high-loading Fe single atoms. Subsequently, continuous catalytic BPA degradation experiments were carried out to examine the stability of Fe-SACs during the reaction (Fig. 4c), which revealed the most robust stability of Fe-N_4-C_6O_2 among the three Fe-SACs, even though its BPA adsorption capacity was not as good as that of Fe-N_2O_2-C_{10} (Fig. 4d). After 120 h of continuous treatment, the iron leaching ratio of Fe-N_4-C_6O_2 was merely 8.0%, much lower than those of Fe-N_2O_2-C_{10} (67.4%) and Fe-N_4-C_{10} (30.5%) (Fig. 4e). Strikingly, the reactivity of Fe-N_4-C_6O_2 did not decline after 240 h of reaction and its structure kept almost unchanged even after 500 h of operation (Supplementary Figs. 21–24 and Table 6). Considering the complexity of pH in different waters, we also monitored the iron leaching of three Fe-SACs under extreme acidic and basic conditions (Fig. 4f), and found that the Fe leaching rate of Fe-N_4-C_6O_2 was even less than that of Fe-N_4-C_{10} at acidic pH and almost the

same as that of Fe-N_4-C_{10} in alkaline solution. Additionally, the demetallation rate of Fe-N_2O_2-C_{10} was much higher than that of Fe-N_4-C_{10}, with a factor of 4.5 or 99 under acidic or alkaline conditions. Therefore, the O doping in the first coordination shell significantly enhanced the activity of single-atom metal sites at the expense of their stability, but a well-balanced relationship between activity and stability of single-atom metal sites could be achieved by rationally designing the Fe-SAC coordination configuration with the O doping in the second coordination shell.

Regarding that the demetallation of Fe-SACs initiates from the elongation and breakage of Fe-N/O bonds, MD simulations were conducted to explore the structure-dependent stability of Fe-SACs in terms of Fe-N/O bond length fluctuations. A relatively shorter Fe-N/O bond length and a narrower range of fluctuations indicate the stable Fe-N/O bonds of the catalyst with less demetallation tendency during reactions. The thermal vibrations of Fe−N/O bond of the Fe-N_2O_2-C_{10}, Fe-N_4-C_6O_2, and Fe-N_4-C_{10} could be visualized in Supplementary Movies 1–3, respectively. As shown in Fig. 4g, h, the radial distribution function (RDF) of Fe-N/O, denoted as $g_{Fe\text{-}N/O}(r)$, was obtained by calculating and counting the frequency of the occurrence of N/O atoms at a distance r from Fe atom. At room temperature, the $g_{Fe\text{-}N}(r)$ of Fe-N_4-C_{10} SAC contained four distinct peaks in the range of 0.875–3.175 Å. However, the fluctuations of N (1.775–3.525 Å) and O (1.775–3.175 Å) in Fe-N_2O_2-C_{10} SAC were farther away from the Fe center, which indicated that the destruction of its symmetric coordination structure weakened the Fe-N and Fe-O bonds, thereby increasing the demetallation tendency. Fascinatingly, the thermal motion amplitude of Fe-N bonds in Fe-N_4-C_6O_2 decreased to 0.925–2.975 Å, revealing its much stronger Fe-N bond to resist external perturbations. These results further illustrated that the O doping in the second coordination shell could reinforce the interaction between Fe single atoms and coordinating N atoms by reducing the electron density of Fe, effectively inhibiting the leaching of Fe atoms during the PMS activation.

Mechanism investigation

We subsequently investigated the reactive species generated in the three Fe-SACs/PMS systems. The contribution of superoxide radicals ($O_2^{\bullet-}$) to the BPA degradation was first excluded through the superoxide dismutase (SOD) quenching experiments and electron paramagnetic resonance (EPR) measurements (Fig. 5a and Supplementary Fig. 25a). The presence of methanol (MeOH) only slightly inhibited the BPA degradation in the three Fe-SACs/PMS systems, indicative of weak contribution of $SO_4^{\bullet-}$ and •OH to the BPA degradation (Fig. 5a and Supplementary Table 7). When using 5,5-dimethyl-1-pyridone-N-oxide (DMPO) as a trapping agent, only a signal of DMPO oxides (DMPOX) was observed in the three Fe-SAC/PMS systems, which might be originated from oxidation of DMPO by $Fe^{IV}=O$ or other non-radical species, without the appearance of •OH and $SO_4^{\bullet-}$ signals (Supplementary Fig. 25b–d). The above results revealed that non-radical oxidation pathways such as electron transfer process (ETP), $Fe^{IV}=O$ or singlet oxygen ($^1O_2$) oxidation mainly took place in these systems, while the inhibitory effect of MeOH may not be solely attributed to the radicals quenching, but to its competitive adsorption on Fe-SACs with BPA and/or its competitive reaction with other ROS, such as $Fe^{IV}=O$[42]. The relatively weak inhibition effects of methyl phenyl sulfoxide (PMSO) on Fe-N_4-C_{10}/PMS (35.1%) and Fe-N_2O_2-C_{10}/PMS (36.8%) systems suggested the dominant role of ETP or $^1O_2$ oxidation process, rather than the $Fe^{IV}=O$ oxidation, in these two systems. Surprisingly, PMSO was found to suppress 84.1% of BPA degradation in the Fe-N_4-C_6O_2/PMS system, demonstrating that the doping of O in the second coordination shell could shift the BPA degradation pathway from the ETP or $^1O_2$ oxidation process to the $Fe^{IV}=O$ counterpart. Furthermore, the MeOH and PMSO quenching experiments further confirmed that $Fe^{IV}=O$ was the dominant species for the degradation of 2, 4-DCP, 4-CP, PE, PNP, FP, PNBD, and PNBA (Supplementary Figs.26–28). Notably, the higher degradation rates of electron-rich phenolic pollutants in this system were attributed to their high electron density environment, which facilitated the electrophilic attack by $Fe^{IV}=O$[43,44]. Given that the reactions of PMSO with •OH, $SO_4^{\bullet-}$ and $Fe^{IV}=O$ would form different products (Eqs. S15–S17), where PMSO can be oxidized to methyl phenyl sulfone ($PMSO_2$) through the oxygen atom transfer (OAT) pathway by $Fe^{IV}=O$, we utilized the PMSO oxidation to further check the generation of radicals and $Fe^{IV}=O$[45]. It was observed that the consumption of PMSO in the Fe-N_2O_2-C_{10}/PMS system was significantly lower than that in the Fe-N_4-C_{10}/PMS and Fe-N_4-C_6O_2/PMS systems, suggesting that *PMS was the primary reactive species in the Fe-N_2O_2-C_{10}/PMS system, rather than radicals and $Fe^{IV}=O$ (Supplementary Fig. 29). Meanwhile, the conversion of $PMSO_2$ in the Fe-N_4-C_{10}/PMS and Fe-N_4-C_6O_2/PMS systems was close to 100%, confirming that $Fe^{IV}=O$ was predominantly generated in these two systems rather than radicals. Furthermore, an isotropic signal at $g = 2.0025/2.0027$, attributed to the Fe $3d^5$ orbitals with large zero-field splitting and unpaired electrons, was detected in the Fe-N_4-C_6O_2 and Fe-N_4-C_{10} systems. This EPR signal was enhanced and also shifted to a lower value by the PMS activation, reconfirming the presence of $Fe^{IV}=O$ (Fig. 5b)[13].

Subsequently, we investigated the ETP and the $^1O_2$ oxidation processes in the three Fe-SACs/PMS systems. The addition of 2, 2, 6, 6-tetramethylpiperidine (TEMP) did not significantly inhibit the BPA degradation (Fig. 5a), and the replacement of H_2O with D_2O did not enhance the 2, 2, 6, 6-tetramethylpiperidine-N-oxyl (TEMPO) signal (Supplementary Fig. 30), indicating the negligible contribution of $^1O_2$[46]. After excluding radicals and $Fe^{IV}=O$ interference, the pH-dependent degradation rate changes of BPA and 2, 4-DCP in the Fe-SACs/PMS system were completely different from those in the $^1O_2$ oxidation system (Supplementary Fig. 31). These results ruled out the $^1O_2$ generation[28,47]. Subsequently, in-situ Raman spectroscopy and chronopotentiometry tests were conducted to further check the interaction between Fe sites and PMS, as well as the electron transfer processes (Supplementary Fig. 32). We observed three distinct peaks at 880, 980, and 1061 cm^{-1} in the PMS solution, corresponding to the stretching vibrations of O-O, SO_4^{2-}, and SO_3^{-}, respectively[16]. The O-O and SO_3^{-} peaks decreased drastically, while SO_4^{2-} peaks increased significantly upon addition of Fe-SACs, indicating the rapid PMS activation. Meanwhile, two new peaks emerged at 820 cm^{-1} and 840 cm^{-1}, along with a red-shift of the SO_3^{-} characteristic peak, suggesting the formation of *PMS complexes and $Fe^{IV}=O$, as well as electron donation from Fe sites to PMS[48,49], which were further confirmed by the first increased and subsequent decreased trend of open-circuit potential of Fe-SAC electrode upon the addition of PMS and BPA[50]. Consequently, we conclude that the ETP pathway engaged in the BPA degradation in the three Fe-SACs/PMS systems, where Fe-SACs mediate the electron transfer from BPA to PMS. Notably, Fe-N_2O_2-C_{10} and Fe-N_4-C_6O_2 possessed the stronger potential fluctuations than Fe-N_4-C_{10} after the addition of PMS and BPA, suggesting that the O doping in either the first or second coordination shell could promote the ETP. This is because the doped O could reduce the energy of the lowest unoccupied molecular orbital (LUMO) in the *PMS complexes by modulating the molecular orbital energy levels and electron distributions of the Fe-SACs, which narrowed the energy gap with the highest occupied molecular orbital (HOMO) of BPA, thus effectively facilitating the transfer of electrons from BPA to PMS (Supplementary Fig. 33).

We then quantified the steady-state concentrations of different ROS through measuring the competition kinetics between ROS and probe compounds to deeply investigate the effect of O doping in the second coordination shell on the catalytic process and the $Fe^{IV}=O$ reactivity (Fig. 5c–e, Supplementary Fig. 34, Tables 8–9). As illustrated in Fig. 5c, the steady-state concentrations of $Fe^{IV}=O$ produced in the Fe-N_4-C_{10}/PMS and Fe-N_4-C_6O_2/PMS system were 1.09×10^{-6} and

https://doi.org/10.1038/s41467-025-57643-7

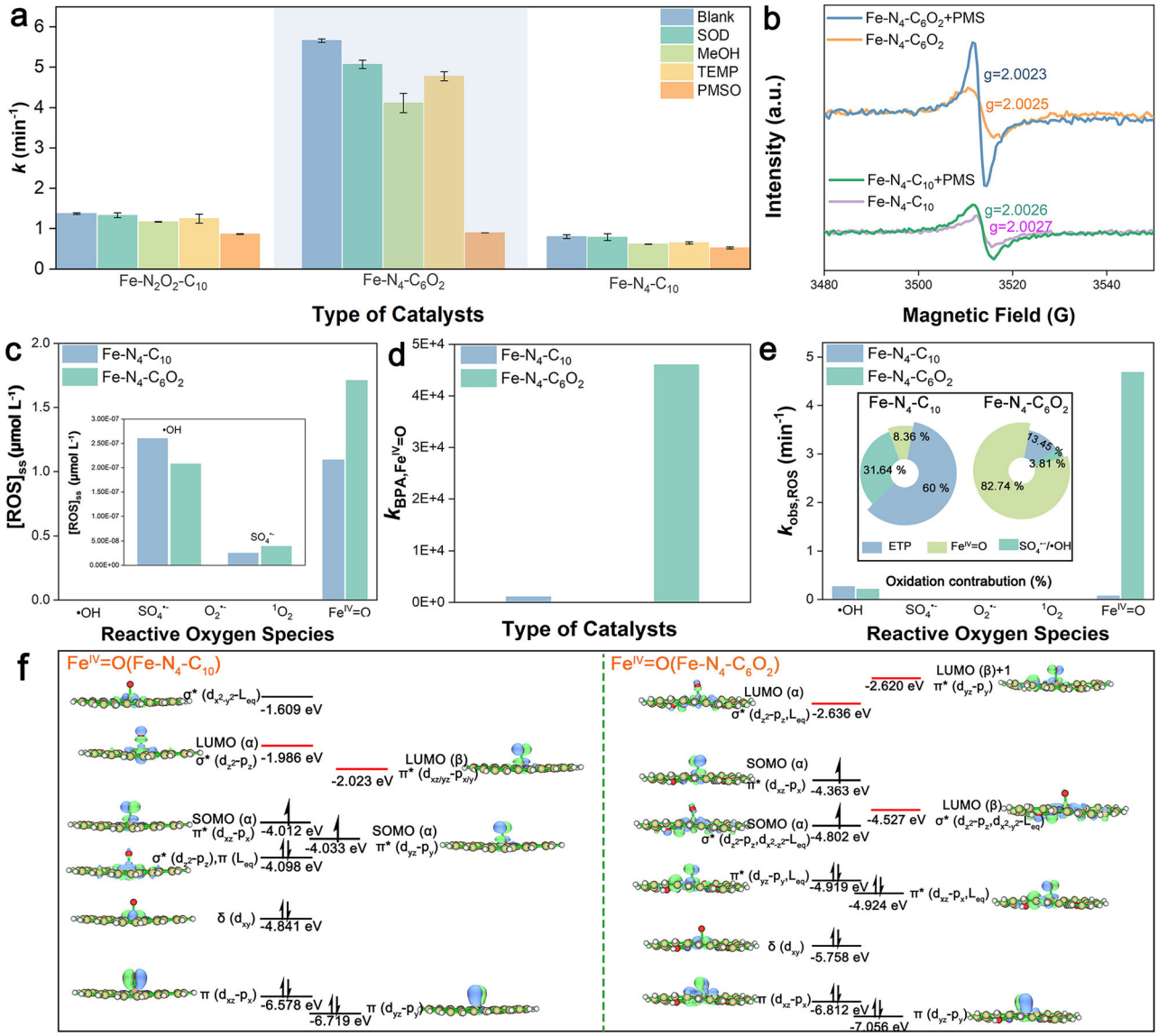

Fig. 5 | Mechanistic interrogation of Fe-SACs/PMS system: identification of reactive species and simulation of Fe^{IV} = O electronic structure. a Effect of scavengers on BPA degradation in the Fe-SACs/PMS system. The error bars represent the standard deviation derived from two repeated experiments. Experimental conditions: [BPA] = 50 μM, [catalysts] = 0.05 g L^{-1}, $[PMS]_0$ = 400 μM, T = 25 °C, pH = 7, [SOD] = 100 U mL^{-1}, [MeOH/PMS] = 1000, [PMSO/PMS] = 100, [TEMP] = 0.24 mM. **b** EPR spectra of Fe-SACs and Fe-SACs/PMS. **c** The steady-state concentrations of different ROS in the Fe-SACs/PMS system (inset: the steady-state concentrations of •OH and $SO_4^{\bullet-}$). **d** The second-order reaction rate between BPA and Fe^{IV} = O in the Fe-SACs/PMS system. **e** The observed reaction rate constants of ROS and BPA in the Fe-SACs/PMS system (inset: the oxidation contributions of different ROS to BPA degradation). **f** The molecular orbital composition and energy level of Fe^{IV} = O[57]. The above illustration displays only the orbitals in the vicinity of the LUMO orbital. The N-Fe-N axis in Fe^{IV} = O(Fe-N_4-C_6O_2) where N is directly connected to O is defined as the x-axis. Source data are provided as a Source Data file.

1.71×10^{-6} mol L^{-1}, respectively, which were 7–8 orders of magnitude higher than that of •OH and $SO_4^{\bullet-}$, strongly validating that Fe-N_4-C_{10}/PMS and Fe-N_4-C_6O_2/PMS were more likely to produce Fe^{IV} = O species rather than radicals, consistent with theoretical predictions. However, the second-order reaction rate constant of Fe^{IV} = O species produced in the Fe-N_4-C_{10}/PMS system with BPA was only 1.08×10^3 M^{-1} s^{-1}, much lower than that of the radicals (1.37×10^9–1.7×10^{10} M^{-1} s^{-1})[51–53], rendering the contribution of Fe^{IV} = O to the BPA oxidation to be only 8.4%, much lower than those of ETP (60.0%) and radical oxidation (31.6%) (Fig. 5d, e and Supplementary Tables 8–9). These facts suggested that the Fe^{IV} = O species produced in the Fe-N_4-C_{10}/PMS system possessed low reactivity towards BPA. Surprisingly, the second-order reaction rate constant of Fe^{IV} = O species produced in the Fe-N_4-C_6O_2/PMS system with BPA increased to 4.6×10^4 M^{-1} s^{-1}, 41.6-fold that of Fe-N_4-C_{10}/PMS (Fig. 5d), suggesting that the O doping in the second coordination shell could significantly increase the reactivity of Fe^{IV} = O towards BPA. Consequently, the contribution of Fe^{IV} = O to the BPA removal sharply increased to 82.74% in the Fe-N_4-C_6O_2/PMS system.

Theoretically, either π*($d_{xz/yz}$-$p_{x/y}$) or σ*(d_{Z^2}-p_z) antibonding orbitals at the Fe = O fragment in Fe^{IV} = O could receive foreign electrons to disrupt the Fe=O bond, triggering the terminal O transfer and the substrate oxidation (Supplementary Fig. 35a). The Mössbauer spectroscopy indicated the O doping and the CVs generation could significantly increase the spin state of Fe-N_4-C_6O_2 (Supplementary Fig. 35b). According to the ligand field theory, the metal center typically possesses a high spin state when it is coordinated with a weak-field ligand and vice versa. Therefore, the enhanced spin state indicated that the O doping and the CVs generation could effectively weaken the strength of coordination field, resulting in a decrease in the energy of the Fe 3d orbitals to further reduce the orbital energy of

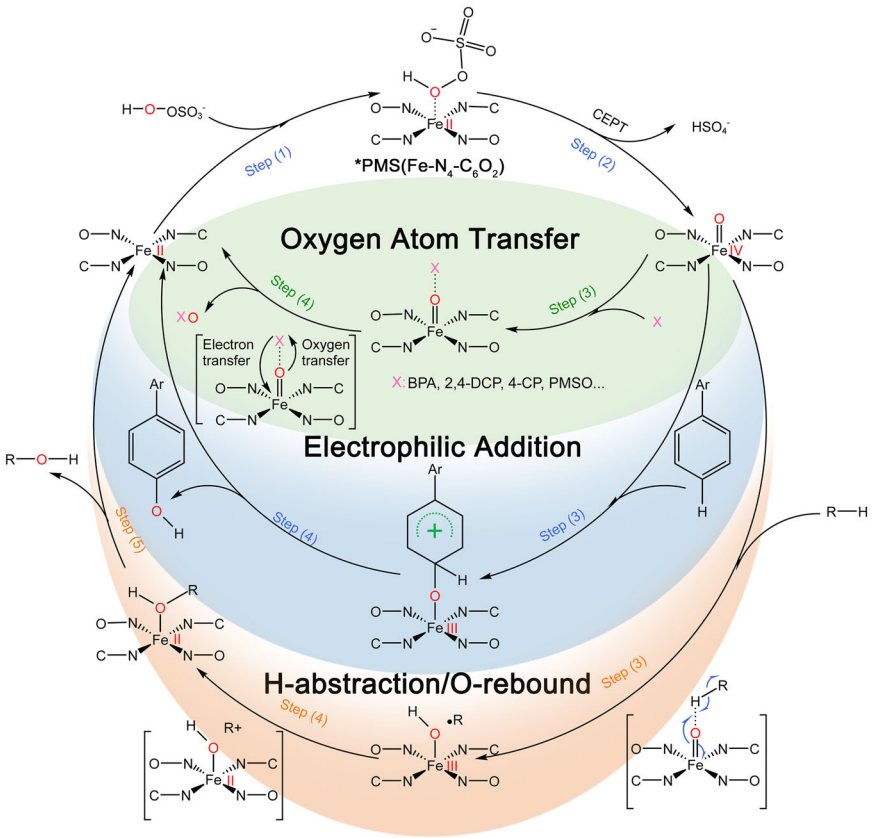

Fig. 6 | Reaction mechanisms diagram of $Fe^{IV}=O$ with pollutants. The $Fe^{IV}=O$ species oxidizes pollutants through the OAT reaction, electrophilic addition, and H-abstraction/O-rebound mechanism.

Fe=O fragment in $Fe^{IV}=O$, and improving the oxidative reactivity of $Fe^{IV}=O$. Subsequently, we employed DFT calculations to clarify the increased intrinsic reactivity of $Fe^{IV}=O$ produced in the Fe-N_4-C_6O_2/PMS system. As shown in Fig. 5f, the $Fe^{IV}=O$ produced in the Fe-N_4-C_{10}/PMS system possessed the π- and σ-attack pathways for the pollutants oxidation. Its Fe/O ($d_{xz/yz}$-p_x/p_y) π* (β) orbitals (-2.023 eV) and (d_{z^2}-p_z) σ* (α) orbitals (−1.986 eV) could accept electrons from pollutant substrates, thereby reducing the bond order of Fe=O and favoring the terminal O transfer. In the π-attack pathway, the pollutants needed to overlap orbitals from a direction perpendicular to the Fe=O bond, which resulted in a spatial collision between the pollutants and the equatorial ligands of $Fe^{IV}=O$ produced in the Fe-N_4-C_{10}/PMS system. In the σ-attack pathway, its (d_{z^2}-p_z) σ* (α) orbital had a high energy (−1.986 eV), requiring a considerable energy barrier to be overcome to initiate σ-attack. Overall, the two reaction pathways of $Fe^{IV}=O$ produced in the Fe-N_4-C_{10}/PMS system exhibited moderate reactivity towards pollutant. For the $Fe^{IV}=O$ produced in the Fe-N_4-C_6O_2/PMS system, the orbital components became more complicate and the orbital energy levels were significantly lowered due to the doping of oxygen atoms and the decrease of ligand field intensity. Among them, the energies of its (d_{z^2}-p_z, $d_{x^2-y^2}$_Leq) σ* (β) and (d_{z^2}-p_z, Leq) σ* (α) orbitals were respectively reduced to −4.527 eV and −2.636 eV, significantly lower than that of its (d_{yz}-p_y) π* (β) orbital (−2.620 eV). As a result, the electrons of the pollutant could fill the low-lying σ* orbitals of $Fe^{IV}=O$ produced in the Fe-N_4-C_6O_2/PMS system along the Z-axis without steric hindrance, which facilitated the formation of the pollutant-O-Fe collinear transition state, thereby accelerating the reaction between the pollutant with $Fe^{IV}=O$.

Finally, we determined the main intermediates in the degradation process by liquid chromatography-mass spectrometry (LC-MS) and gas chromatography-mass spectrometry (GC-MS) techniques (Supplementary Figs. 36–39, Tables 10–11), and proposed two potential BPA degradation pathways in the Fe-N_4-C_6O_2/PMS system (Supplementary Fig. 40, details can be found in the Supporting Information). In these two pathways, BPA was oxidized by $Fe^{IV}=O$ through the OAT reaction, electrophilic addition, and H-abstraction/O-rebound mechanisms (Fig. 6). The core of these three oxidation mechanisms was the filling of pollutant electrons into the low-lying σ* orbitals of Fe/O to form pollutant-O-Fe intermediates, thus realizing the oxidation of pollutant and the reduction of $Fe^{IV}=O$. Notably, the decrease of total organic carbon (TOC) in BPA solution reached as high as 90% in 2 min when the concentration of Fe-N_4-C_6O_2 SAC was 0.1 g L^{-1}, and it was close to 80% in 2 min even when the catalyst concentration was reduced by half (Supplementary Fig. 41), which indicated that the Fe-N_4-C_6O_2 SAC exhibited a good performance in AOPs, which was able to cause the organic compounds to be degraded into harmless ones completely and reduce the environment impact.

Discussion

In summary, we reported the synthesis of Fe-N_4-C_6O_2 SAC by substituting C in the second coordination shell of Fe-N_4 sites with O and demonstrated Fe-N_4-C_6O_2 sites could activate PMS more efficiently and stably by providing an enhanced localized electric field without destroying their symmetric coordination structure in the first coordination shell. The O doping in the second coordination shell could enhance the strength of the Fe-N bond by reducing the electron density of Fe center and weaken the amplitude of Fe-N bond during the PMS activation, therefore effectively preventing the demetallation of Fe-N_4 sites. More importantly, this O doping also lowered the energy of Fe=O σ* orbitals by weakening the coordination field to promote the electrophilic σ-attack of $Fe^{IV}=O$ towards electron-rich contaminants. This work sheds light on the importance of second coordination shell doping in enhancing the stability of Fe-N_4 SAC and offers a design

strategy to address the trade-off between high activity and durable stability in SAC preparation.

Methods

Materials and chemicals

Oxone ($2KHSO_5{\cdot}KHSO_4{\cdot}K_2SO_4$, active oxygen ≥ 4.50%) and BPA (AR) were supplied by Shanghai Aladdin Biochemical Technology Co., Ltd (Shanghai, China) and Sinopharm Chemical Reagent Co., Ltd (Shanghai, China), respectively. Details of the other chemicals are presented in Supplementary Method 1. All chemicals were used as received and dissolved by ultrapure water (18.25 MΩ cm^{-1}).

Catalyst preparation

For the synthesis of Fe-N_4-C_6O_2 SAC, $FeCl_2{\cdot}4H_2O$ (0.5 mmol) and 10-phenanthroline monohydrate (2 mmol) were ultrasonically dispersed in 60 mL absolute ethanol to obtain Fe-N coordination complex (I). Then, SiO_2@RF (3 g) was added to the solution and stirred under reflux at 60 °C for 4 h. Next, the pre-prepared complex (I) was deposited on SiO_2@RF by reduced pressure evaporation at 50 °C. The dried solid was then heated to 700 °C (calcined for 2 h) at a rate of 2 °C min^{-1} in an N_2 atmosphere. Subsequently, the resulting black solid was dispersed into 100 mL 5 wt % HF and stirred at room temperature for 4 h to remove SiO_2. This procedure was repeated three times. Afterward, the solid was washed repeatedly with a large amount of ultrapure water until the filtrate reached neutral pH. Finally, the dried black powder was recorded as Fe-N_4-C_6O_2 SAC. For the synthesis of Fe-N_2O_2-C_{10} SAC, the steps remained consistent with those of Fe-N_4-C_6O_2 except that 10-phenanthroline monohydrate and SiO_2@RF were replaced by (S,S)-(+)-N,N′-bis(3,5-di-tert-butylsalicylidene)-1,2-cyclohexanediamin and SiO_2@N-C, respectively. For the synthesis of Fe-N_4-C_{10}, the steps remained consistent with those of Fe-N_4-C_6O_2 except for the deposition of complex (I) on SiO_2.

The synthesis of carriers (SiO_2, SiO_2@RF, and SiO_2@N-C) and other catalysts (Fe-NPs/NC, N/O-C, and N-C) were included in Supplementary Method 2. The specific amounts of each reagent used in the catalyst synthesis process are presented in Supplementary Table 1.

Characterization of the catalysts

The characterization methods including Field emission scanning electron microscope (FESEM), HR-TEM, PXRD, XPS, Raman, inductively coupled plasma optical emission spectrometry (ICP-OES), Brunauer-Emmett-Teller (BET), AC-HAADF STEM, X-ray absorption spectra (XAS), EPR, and ^{57}Fe Mössbauer spectroscopy are described in Supplementary Method 3.

Experiment procedures

The degradation experiments of BPA, as well as the effects of PMS dosages (100–500 μM), catalyst dosages (0.01, 0.02, 0.05, 0.1 mg mL^{-1}), pH (pH = 2–10) coexisting ions (Cl^-, HCO_3^-), and quenchers on BPA degradation are described in Supplementary Method 4.

Analytical methods

The analytical methods for the target compounds, including liquid chromatography (LC), liquid chromatography-mass spectrometry (LC-MS), and gas chromatography-mass spectrometry (GC-MS), are detailed in Supplementary Method 5.

EPR analysis for $Fe^{IV}=O$

20 mg of Fe SAC was mixed with 50 μL of pure water or saturated PMS solution, and subsequently transferred to a quartz tube for EPR analysis. All EPR tests were performed at 77k.

Calculation formula

The calculation formulas for apparent rate constants (k), TOF, k-value, and TOC are presented in Supplementary Method 6.

Electrode preparation

The preparation method for the Fe-SAC electrode is detailed in Supplementary Method 7.

Steady-state concentration and contribution of ROS

The experimental methods and formula derivation for the quantitative assessment of ROS steady-state concentration and their contribution to BPA degradation are detailed in Supplementary Method 8.

Long-term stability test

The Fe-SAC suspension was deposited on a Mixed Cellulose Esters (MCE) membrane (pore size = 0.45 μm, D.25 mm) through filtration and then placed in a filter (i.D. 25 mm). The effective membrane area of the Fe-SAC/MCE composite microfiltration membrane is 1.33 cm^2 and the loading capacity of the catalyst is 15.03 mg cm^{-2}. Next, the Fe-SAC/MCE filter and peristaltic pump are used to form a continuous flow reactor to evaluate the long-term stability of Fe-SAC.

Theoretical

The theoretical calculations were performed using Gaussian 16 software[54] and Multiwfn 3.8 program[55,56] on the basis of DFT. The dynamic simulations elucidating the material's dynamic behaviors were conducted through the application of Born–Oppenheimer molecular dynamics (BOMD) simulations, as implemented within the openly accessible CP2K/Quickstep package (Supplementary Method 9).

Data availability

All study data are included in the article and Supplementary Information. Source data are provided with this paper.

References

1. Yao, Y. et al. Rational regulation of Co-N-C coordination for high-efficiency generation of $^1O_2$ toward nearly 100% selective degradation of organic pollutants. *Environ. Sci. Technol.* **56**, 8833–8843 (2022).
2. Zhang, L. S. et al. Carbon nitride supported high-loading Fe single-atom catalyst for activation of peroxymonosulfate to generate $^1O_2$ with 100 % selectivity. *Angew. Chem. Int. Ed.* **60**, 21751–21755 (2021).
3. Wang, J. et al. Facile synthesis of atomic Fe-N-C materials and dual roles investigation of Fe-N_4 sites in Fenton-like reactions. *Adv. Sci.* **8**, 2101824 (2021).
4. Xiong, Y. et al. Single-atom Fe catalysts for Fenton-like reactions: roles of different N species. *Adv. Mater.* **34**, e2110653 (2022).
5. Huang, B. et al. Coupled surface-confinement effect and pore engineering in a single-Fe-atom catalyst for ultrafast Fenton-like reaction with High-Valent Iron-Oxo complex oxidation. *Environ. Sci. Technol.* **57**, 15667–15679 (2023).
6. Gao, Y. et al. Unraveling the high-activity origin of single-atom iron catalysts for organic pollutant oxidation via peroxymonosulfate activation. *Environ. Sci. Technol.* **55**, 8318–8328 (2021).
7. Chen, Q. et al. Atomically dispersed Fe/Bi dual active sites single-atom nanozymes for cascade catalysis and peroxymonosulfate activation to degrade dyes. *J. Hazard. Mater.* **422**, 126929 (2022).
8. Li, X. et al. CoN_1O_2 single-atom catalyst for efficient peroxymonosulfate activation and selective Cobalt(IV)=O generation. *Angew. Chem. Int. Ed.* **62**, e202303267 (2023).
9. Cui, J. et al. Regulating the metal–support interaction: double jump to reach the efficiency apex of the Fe-N_4-catalyzed Fenton-like reaction. *ACS Catal.* **12**, 14954–14963 (2022).
10. Chen, Y., Zhang, G., Liu, H. & Qu, J. Confining free radicals in close vicinity to contaminants enables ultrafast fenton-like processes in the interspacing of MoS_2 membranes. *Angew. Chem. Int. Ed.* **58**, 8134–8138 (2019).

11. Kuang, J., Guo, H., Si, Q., Guo, W. & Ma, F. Nitrogen vacancies regulated the local electron density of iron sites in g-C_3N_4 to boost the generation of high-valent iron-oxo species in a peracetic acid-based Fenton-like process. *Appl. Catal. B Environ.* **337**, 122990 (2023).
12. Yang, T., Fan, S., Li, Y. & Zhou, Q. Fe-N/C single-atom catalysts with high density of Fe-N_x sites toward peroxymonosulfate activation for high-efficient oxidation of bisphenol A: electron-transfer mechanism. *Chem. Eng. J.* **419**, 129590 (2021).
13. Zhang, B., Li, X., Akiyama, K., Bingham, P. A. & Kubuki, S. Elucidating the mechanistic origin of a spin state-dependent FeN_x-C catalyst toward organic contaminant oxidation via peroxymonosulfate activation. *Environ. Sci. Technol.* **56**, 1321–1330 (2022).
14. Chu, C. et al. Cobalt single atoms on tetrapyridomacrocyclic support for efficient peroxymonosulfate activation. *Environ. Sci. Technol.* **55**, 1242–1250 (2021).
15. Zhou, X. et al. Identification of Fenton-like active Cu sites by heteroatom modulation of electronic density. *Proc. Natl. Acad. Sci. USA* **119**, e2119492119 (2022).
16. Cheng, C. et al. Generation of Fe(IV)=O and its contribution to Fenton-like reactions on a single-atom iron-N-C Catalyst. *Angew. Chem. Int. Ed.* **62**, e202218510 (2023).
17. Pan, Y. et al. Regulating the coordination structure of single-atom Fe-N_xC_y catalytic sites for benzene oxidation. *Nat. Commun.* **10**, 4290 (2019).
18. Wang, B. et al. A site distance effect induced by reactant molecule matchup in single-atom catalysts for Fenton-like reactions. *Angew. Chem. Int. Ed.* **61**, e202207268 (2022).
19. Miao, J. et al. Single-Atom MnN_5 catalytic sites enable efficient peroxymonosulfate activation by forming highly reactive Mn(IV)-Oxo Species. *Environ. Sci. Technol.* **57**, 4266–4275 (2023).
20. Zhou, Z. et al. Fe-based single-atom catalysis for oxidizing contaminants of emerging concern by activating peroxides. *J. Hazard. Mater.* **418**, 126294 (2021).
21. Song, J. et al. Asymmetrically coordinated CoB_1N_3 moieties for selective generation of high-valence Co-Oxo species via coupled Electron-Proton Transfer in Fenton-like reactions. *Adv. Mater.* **35**, e2209552 (2023).
22. Dai, H. et al. Regulating electronic structure of Fe single-atom site by S/N dual-coordination for efficient Fenton-like catalysis. *J. Hazard. Mater.* **465**, 133399 (2024).
23. Peng, L., Duan, X., Shang, Y., Gao, B. & Xu, X. Engineered carbon supported single iron atom sites and iron clusters from Fe-rich Enteromorpha for Fenton-like reactions via nonradical pathways. *Appl. Catal. B Environ.* **287**, 119963 (2021).
24. Li, J. et al. Atomically dispersed Fe atoms anchored on S and N-codoped carbon for efficient electrochemical denitrification. *Proc. Natl. Acad. Sci. USA* **118**, e2105628118 (2021).
25. Chen, S. et al. Unveiling the proton-feeding effect in sulfur-doped Fe-N-C single-atom catalyst for enhanced CO_2 electroreduction. *Angew. Chem. Int. Ed.* **61**, e202206233 (2022).
26. Li, Q. et al. Fe isolated single atoms on S, N codoped carbon by copolymer pyrolysis strategy for highly efficient oxygen reduction reaction. *Adv. Mater.* **30**, e1800588 (2018).
27. Wang, J. et al. Suppressing local charge symmetry of iron single atoms for efficient electrocatalytic nitrate reduction to ammonia ORR. *Adv. Funct. Mater.* **33**, 2304277–2304285 (2023).
28. Xu, H. et al. Improving PMS oxidation of organic pollutants by single cobalt atom catalyst through hybrid radical and non-radical pathways. *Appl. Catal. B Environ.* **263**, 118350 (2020).
29. Wang, J. et al. Suppressing thermal migration by fine-tuned metal-support interaction of iron single-atom catalyst for efficient ORR. *Adv. Funct. Mater.* **33**, 2304277–2304285 (2023).
30. Miao, Q. et al. CoN_2O_2 sites in carbon nanosheets by template-pyrolysis of COFs for CO_2RR. *Chem. Eng. J.* **450**, 138427 (2022).
31. Wang, Z. et al. Cobalt single atoms anchored on oxygen-doped tubular carbon nitride for efficient Peroxymonosulfate activation: simultaneous coordination structure and morphology modulation. *Angew. Chem. Int. Ed.* **61**, e202202338 (2022).
32. Tan, Z. et al. Highly efficient electrocatalysis of oxygen to hydroxyl radical by FeN_2O_2 single-atom catalyst for refractory organic pollutant removal. *Appl. Catal. B-Environ. Energy* **355**, 124170 (2024).
33. Kramm, U. I. et al. Structure of the catalytic sites in Fe/N/C-catalysts for O_2-reduction in PEM fuel cells. *Phys. Chem. Chem. Phys.* **14**, 11673–11688 (2012).
34. Wang, Z. L. et al. Gelatin-derived sustainable carbon-based functional materials for energy conversion and storage with controllability of structure and component. *Sci. Adv.* **1**, e1400035 (2015).
35. Kramm, U. I., Lefevre, M., Larouche, N., Schmeisser, D. & Dodelet, J. P. Correlations between mass activity and physicochemical properties of Fe/N/C catalysts for the ORR in PEM fuel cell via 57Fe Mossbauer spectroscopy and other techniques. *J. Am. Chem. Soc.* **136**, 978–985 (2014).
36. Kramm, U. I. et al. Influence of the electron-density of FeN_4-centers towards the catalytic activity of pyrolyzed FeTMPPCl-based ORR-electrocatalysts. *J. Electrochem. Soc.* **158**, B69–B78 (2011).
37. Shi, L. et al. Photoassisted construction of holey defective g-C_3N_4 photocatalysts for efficient visible-light-driven H_2O_2 production. *Small* **14**, 1703142 (2018).
38. Zhang, X. et al. Unraveling the dual defect sites in graphite carbon nitride for ultra-high photocatalytic H_2O_2 evolution. *Energ. Environ. Sci.* **15**, 830–842 (2022).
39. Hammer, B. & Norskov, J. K. Why gold is the noblest of all the metals. *Nature* **376**, 238–240 (1995).
40. Liu, J., Guo, Y., Fu, X., Luo, J. & Zhi, C. Strengthening absorption ability of Co–N–C as efficient bifunctional oxygen catalyst by modulating the d band center using MoC. *Green Energy Environ.* **8**, 459–469 (2023).
41. Wu, Q. Y., Yang, Z. W., Wang, Z. W. & Wang, W. L. Oxygen doping of cobalt-single-atom coordination enhances peroxymonosulfate activation and high-valent cobalt-oxo species formation. *Proc. Natl. Acad. Sci. USA* **120**, e2219923120 (2023).
42. Zhao, J., Sun, X., Huang, X. & Li, J. Reaction mechanisms of methanol oxidation by $Fe^{IV}O$ biomimetic complex. *Int. J. Quantum Chem.* **116**, 692–701 (2016).
43. Yang, M. et al. Unveiling the origins of selective oxidation in single-atom catalysis via Co-N_4-C intensified radical and nonradical pathways. *Environ. Sci. Technol.* **56**, 11635–11645 (2022).
44. Chen, Y. et al. Facile fabrication of rGO/PPy/nZVI catalytic microreactor for ultrafast removal of p-nitrophenol from water. *Appl. Catal. B Environ.* **324**, 122270 (2023).
45. Pestovsky, O. & Bakac, A. Aqueous Ferryl(IV) Ion: kinetics of oxygen atom transfer to substrates and oxo exchange with solvent water. *Inorg. Chem.* **45**, 814–820 (2006).
46. Ji, J. et al. Defects on CoS_{2-x}: tuning redox reactions for sustainable degradation of organic pollutants. *Angew. Chem. Int. Ed.* **60**, 2903–2908 (2021).
47. Gorman, A. & Rodgers, M. Singlet molecular oxygen. *Chem. Soc. Rev.* **10**, 205–231 (1981).
48. Mo, F. et al. The optimized Fenton-like activity of Fe single-atom sites by Fe atomic clusters-mediated electronic configuration modulation. *Proc. Natl. Acad. Sci. USA* **120**, e2300281120 (2023).
49. Miao, J. et al. Spin-state-dependent peroxymonosulfate activation of single-atom M–N Moieties via a radical-free pathway. *ACS Catal.* **11**, 9569–9577 (2021).
50. Yun, E. T., Lee, J. H., Kim, J., Park, H. D. & Lee, J. Identifying the nonradical mechanism in the peroxymonosulfate activation process: singlet oxygenation versus mediated electron transfer. *Environ. Sci. Technol.* **52**, 7032–7042 (2018).

51. Sanchez, P. M., Ocampo-Pérez, R., Rivera-Utrilla, J. & Mota, A. J. Comparative study of the photodegradation of bisphenol A by HO•, $SO_4^{\bullet-}$ and $CO_3^{\bullet-}$/HCO_3• radicals in aqueous phase. *Sci. Total Environ.* **463**, 423–431 (2013).
52. Ding, J. et al. Electrochemical activation of persulfate on BDD and DSA anodes: electrolyte influence, kinetics and mechanisms in the degradation of bisphenol A. *J. Hazard. Mater.* **388**, 121789 (2020).
53. Ren, W. et al. Origins of electron-transfer regime in persulfate-based nonradical oxidation processes. *Environ. Sci. Technol.* **56**, 78–97 (2021).
54. Frisch, M. J. et al. Gaussian 16, Revision A.03. *Gaussian, Inc., Wallingford CT* (2016).
55. Lu, T. & Chen, F. W. Multiwfn: a multifunctional wavefunction analyzer. *J. Comput. Chem.* **33**, 580–592 (2012).
56. Lu, T. A comprehensive electron wavefunction analysis toolbox for chemists, Multiwfn. *J. Chem. Phys.* **161**, 082503 (2024).
57. Lu, T. & Chen, F. W. Calculation of molecular orbital composition. *Acta Chim. Sin.* **69**, 2393 (2011).

Acknowledgements

This work was financially supported by the National Key Research and Development Program of China (2023YFC3708002), the National Natural Science Foundation of China (U22A20402, 22076059, 22376076, 22076061, 21936003), International Joint Research Center for Intelligent Biosensing Technology and Health, Shenzhen Science and Technology Program (JCYJ20220818095601002), and the Fundamental Research Funds for the Central Universities (CCNU22JC014, CCNU24JL011).

Author contributions

H.X. and L.Z. supervised the project and provided financial support. T.C. conceived and designed the experiments. G.Z. performed DFT calculations and its analysis. T.C., H.X., H.S., G.Z., and L.Z. wrote the paper. Y.H., S.Y., D.Z., H.D., Y.X., and S.H. provided experimental assistance.

Competing interests

The authors declare no competing interests.

Additional information

Supplementary information The online version contains supplementary material available at https://doi.org/10.1038/s41467-025-57643-7.

Correspondence and requests for materials should be addressed to Ganbing Zhang, Hui Xu or Lizhi Zhang.

Peer review information *Nature Communications* thanks the anonymous reviewers for their contribution to the peer review of this work. A peer review file is available.